Research Square

Preprints are preliminary reports that have not undergone peer review.
They should not be considered conclusive, used to inform clinical practice,
or referenced by the media as validated information.

Statistical benchmarking of bromide perovskite radiation detectors using industry-relevant performance metrics

Makhsud Saidaminov
msaidaminov@uvic.ca
University of Victoria https://orcid.org/0000-0002-3850-666X
Sergey Dayneko
University of Victoria https://orcid.org/0000-0002-0604-6099
Vishal Yeddu
University of Victoria https://orcid.org/0000-0003-2016-8620
Daniil Konorov
daniilkonorov@gmail.com
Kate Spicer
kate.spicer@shaw.ca
Nicholas Sandor
nsandor@uvic.ca
James Day
jamesday1215@gmail.com
Antoine Pavesic Junior
antoinep@uvic.ca
Aleksandra Gracheva
agracheva@uvic.ca
Saeid Taherion
saeid.taherion@cnl.ca
Magdalena Bazalova-Carter
University of Victoria https://orcid.org/0000-0002-9365-2889

Article

Keywords:

Posted Date: November 23rd, 2026

DOI: https://doi.org/10.21203/rs.3.rs-10408030/v1

License: This work is licensed under a Creative Commons Attribution 4.0 International License.
Read Full License

Additional Declarations: There is **NO** Competing Interest.

Statistical benchmarking of bromide perovskite radiation detectors using industry-relevant performance metrics

Sergey V. Dayneko[1,2], Vishal Yeddu[1,2], Daniil Konorov[2], Kate Spicer[2], Nicholas Sandor[3], James Day[4], Antoine Pavesic Junior[2], Aleksandra I. Gracheva[1,2], Saeid Taherion[4], Magdalena Bazalova-Carter[5] and Makhsud I. Saidaminov[2,3,*]

[1]AY Sensors Inc., Victoria, British Columbia, Canada

[2]Department of Chemistry, University of Victoria, Victoria, British Columbia, Canada.

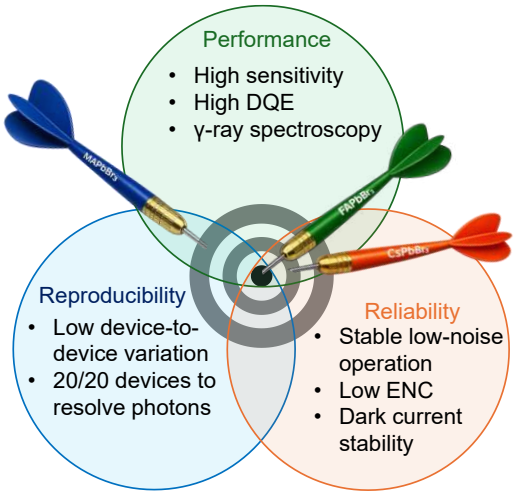
[3]Department of Electrical & Computer Engineering, University of Victoria, Victoria, British Columbia, Canada.

[4]Canadian Nuclear Laboratories, Chalk River, Ontario, Canada

[5]Department of Physics and Astronomy, University of Victoria, Victoria, British Columbia, Canada

E-mail: msaidaminov@uvic.ca

Abstract



Lead halide perovskites have emerged as promising direct-conversion semiconductors for X/γ-ray detection, yet meaningful comparison between reported devices remain challenging because detector architectures, operating conditions, and characterization protocols vary widely, while statistical reproducibility is rarely assessed. Here we present the first statistically robust benchmark of bromide perovskite radiation detectors by comparing 60 detector pixels fabricated from 15 individual single crystals of $MAPbBr_3$, $CsPbBr_3$, and $FAPbBr_3$ using a unified fabrication procedure, device architecture, and measurement conditions. We show that detector performance is governed primarily by the interplay between charge collection efficiency and electronic-noise stability rather than by X-ray absorption, which exceeds 92% for all three compositions under a 70 kVp spectrum. $MAPbBr_3$ exhibits severe field-dependent operational instability and limited carrier transport, restricting operation to 25 V cm^{-1} and yielding a maximum detective quantum efficiency (*DQE*) of only 11.3%. $CsPbBr_3$ achieves efficient charge collection and high *DQE* of 97% but increasingly becomes limited by electronic-noise fluctuations at electric fields above 2,000 V cm^{-1}. In contrast, $FAPbBr_3$ combines high mobility-lifetime products (up to 1.2×10^{-2} cm^2 V^{-1}), low electronic noise ($<3\times10^3$ e^- RMS), X-ray sensitivity approaching the theoretical limit, and near-unity *DQE* under low-dose conditions. Photon-counting γ-ray spectroscopy further identifies $FAPbBr_3$ as the most reproducible perovskite, with all 20 investigated detectors resolving ^{57}Co 122 keV photopeak and achieving a median energy resolution of 6.1±0.7%. Monte Carlo charge-transport modelling indicates that $FAPbBr_3$ detectors, when coupled with lower-noise readout electronics, could approach ~1% energy resolution. By introducing statistically representative, industry-relevant performance benchmarks, this work provides a roadmap for the development of perovskite photon-counting X/γ-ray imagers.

1. Introduction

Lead halide perovskites have emerged as one of the most promising classes of semiconductors for direct-conversion detection of ionizing radiation. Their unique combination of high atomic number, large carrier mobility-lifetime ($\mu\tau$) products, high resistivity and solution-processable crystal growth enables efficient conversion of X-ray and γ-ray photons directly into electrical charge, offering an attractive alternative to conventional detector materials such as silicon, amorphous selenium (a-Se), CdTe, and CdZnTe.[1–9] Recent advances in crystal growth, defect passivation, detector engineering and pixelated device integration have rapidly expanded the application of perovskite detectors from proof-of-concept X-ray sensors to large-area imaging arrays, photon-counting detectors and γ-ray spectrometers for medical imaging and security applications.[10–15]

A key advantage of lead halide perovskites is their ability to form high-quality single crystals by low-temperature solution growth, enabling scalable fabrication of thick direct-conversion detectors without the high-temperature and high-cost crystal-growth processes required for CdZnTe or CdTe.[16–19] Their exceptional defect tolerance, long carrier diffusion lengths, high resistivity and balanced electron and hole transport have enabled remarkable X-ray sensitivity, ultralow detection limits and high-resolution imaging.[20–26] Recent demonstrations of perovskite detector arrays integrated with thin-film electronics and readout circuits further highlight their potential for next-generation photon-counting medical imaging systems.[27–30]

Among lead halide perovskites, bromide-based compositions have attracted attention because their wider bandgaps suppress dark current and reduce ion migration compared with iodide analogs. Consequently, methylammonium lead bromide ($MAPbBr_3$), formamidinium lead bromide ($FAPbBr_3$) and cesium lead bromide ($CsPbBr_3$) have emerged as leading candidates for direct-conversion radiation detectors. Numerous studies have demonstrated high X-ray sensitivity, low detection limits, excellent charge-collection efficiency and γ-ray spectroscopy using these perovskite compositions. Nevertheless, the reported detector performance varies substantially across the literature owing to differences in crystal-growth methods, contact materials, detector geometry, operating electric field and readout electronics.[20]

Despite the rapid progress of the field, meaningful comparison between bromide perovskite detectors remains difficult. Even fundamental detector parameters, including dark current,

mobility-lifetime product, sensitivity and energy resolution, often vary by more than an order of magnitude between different reports. Furthermore, most studies evaluate only one or a few representative devices, making statistical assessment of device-to-device reproducibility impossible. Equally important, detector metrics widely adopted by the medical-imaging community, such as equivalent noise charge (*ENC*), noise-equivalent dose (*NED*), and detective quantum efficiency (*DQE*), are only rarely reported for perovskite detectors, preventing quantitative comparison with established semiconductor detector technologies and limiting assessment of their technological readiness.[20,31]

Here, we address these limitations through a statistically robust comparison of bromide perovskite single-crystal radiation detectors fabricated and characterized under identical experimental conditions. 60 detector pixels fabricated from 15 independent single crystals (5 $MAPbBr_3$, 5 $CsPbBr_3$ and 5 $FAPbBr_3$, each with 4 pixels) were evaluated using a common device architecture and standardized electrical, X-ray and γ-ray characterization protocols. By combining dark-current stabilization analysis, electronic noise characterization, mobility-lifetime measurements, X-ray sensitivity evaluation, empirically informed *DQE(0)* calculation, photon-counting γ-ray spectroscopy and detector-specific Monte Carlo charge-transport simulations, we establish a unified framework for quantitatively comparing bromide perovskite detector materials. The results demonstrate that practical detector performance is governed predominantly by the interplay between carrier transport and electronic-noise stability rather than by X-ray absorption alone, identifying $FAPbBr_3$ as the most balanced bromide perovskite composition for direct-conversion radiation detection, and provide statistically representative performance benchmarks relevant to both academic and industrial detector development.

2. Results and discussion

Detailed procedures on crystal growth and device fabrication are given in the Methods section. Briefly, all single crystals were synthesized via solution-based methods, namely flux-regulation crystallization (FRC) for $MAPbBr_3$ and $CsPbBr_3$, and inverse-temperature crystallization (ITC) for $FAPbBr_3$.[32,33] $MAPbBr_3$ and $FAPbBr_3$ crystals were 2 mm thick, whereas $CsPbBr_3$ crystals ranged from 1 to 2 mm in thickness. Four gold (Au) pixels (1.5×1.5 mm^2) and a guard ring were deposited on one side of each crystal, and the crystals were then mounted on custom-designed printed circuit boards interfacing with gold electrodes (Fig. 1a). Bismuth (Bi) was then deposited

on the opposite side as the counter electrode to complete the devices (Supplementary Fig. 1). For each composition, 5 independent crystals were fabricated, each containing 4 individually addressable pixels, resulting in a total of 20 independent Au/perovskite/Bi detector devices per composition (60 devices in total, Fig. 2a). Table 1 summarizes the statistically derived key material and detector figures of merit, together with the corresponding abbreviations. The complete device-by-device dataset is provided in the Supplementary Spreadsheet. The associated results are discussed below.

Table 1. Statistical comparison of electrical, transport and detector-performance metrics of Au/perovskite/Bi devices.

	Figures of merit	Abbreviation (unit)	$MAPbBr_3$	$CsPbBr_3$	$FAPbBr_3$
Material	Operating field	V, (V cm^{-1})	25	1,000	1,000
	Dark current*	I_{dark} (nA)	2.05 ± 0.70	1.71 ± 0.80	0.25 ± 0.11
	Equivalent noise charge*	ENC (e^- RMS) × 10^3	2.55 ± 0.04	4.46 ± 1.65	2.63 ± 0.07
	Sensitivity*	S (μC Gy_{air}^{-1} cm^{-2}) × 10^3	0.28 ± 0.13	2.85 ± 0.62	3.30 ± 0.32
	Mobility-to-lifetime product**	$(\mu\tau)_h$ (cm^2 V^{-1}) × 10^{-3}	0.96 [0.70-1.47]	1.15 [0.77-11.8]	2.06 [0.98-11.9]
Detector	Maximum $DQE(0)$**	DQE_{max} (%)	11.3 [8.1-17.2]	90.4 [86.1-97.1]	89.3 [84.6-92.9]
	Noise-equivalent dose**	NED (μGy_{air} s^{-1})	11.8 [11.8-104.7]	4.66 [3.88-8.79]	1.60 [1.51-3.2]
	Dose to reach 95% of DQE_{max}**	$D_{0.95DQEmax}$ (μGy_{air} s^{-1})	181.7 [181.7-648.3]	81.4 [69.0-142.9]	29.5 [28.0-57.4]
	Energy resolution for ^{57}Co (%)***	ER_{57Co} (%)	-	14.8, 17.8***	6.1 ± 0.7
	FWHM for ^{57}Co	$FWHM_{57Co}$ (keV)	-	18.1, 21.7***	7.44 ± 0.89

**Values are reported as median ± median absolute deviation (MAD) calculated from independent devices after exclusion of statistical outliers using the 1.5× interquartile range criterion for 20 devices (except for $MAPbBr_3$ sensitivity which was based on 12 devices).*

***Values are reported as median [minimum–maximum] for 3 $MAPbBr_3$ devices, 5 $FAPbBr_3$ devices and 5 $CsPbBr_3$ devices.*

****γ-ray spectroscopy measurements were performed at 4,000 V cm^{-1} for $FAPbBr_3$ devices and 2,000 V cm^{-1} for $CsPbBr_3$ devices. All 20 $FAPbBr_3$ devices exhibited a sufficiently resolved ^{57}Co photopeak, whereas this was observed in only two $CsPbBr_3$ devices.*

$\mu\tau$ products were measured under X-ray irradiation at 40 kVp without filtration.

S, DQE and NED values were evaluated under a filtered 70 kVp X-ray spectrum with a mean photon energy of ~55 keV (0.72 mm Cu + 6 mm Al filtration, source-to-detector distance of 100 cm).

DQE(0) - the detective quantum efficiency at zero spatial frequency.

NED and $D_{0.95DQEmax}$ values are reported as detector dose per image assuming an integration time of 20 ms.

2.1. Dark-current and electronic noise

Dark current (I_{dark}) is commonly evaluated using current-voltage sweeps; however, in perovskites, mobile ions and defect-mediated processes induce transient effects and hysteresis during electrical biasing.[34,35] These processes lead to pronounced temporal I_{dark} fluctuations, which directly contribute to low-frequency electronic noise and degrade detector performance under low X-ray-

dose operating conditions.[13,36] Therefore, current-voltage sweeps are unsuitable for accurately quantifying perovskites' I_{dark}. Instead, following a recent Consensus Statement[34], we report the time evolution of I_{dark} over 600 s under a constant electric field (Figs. 1b-d), together with frequency-dependent electronic-noise (Supplementary Fig. 2) and equivalent noise charge (*ENC*) distributions for all devices (Supplementary Fig. 3).

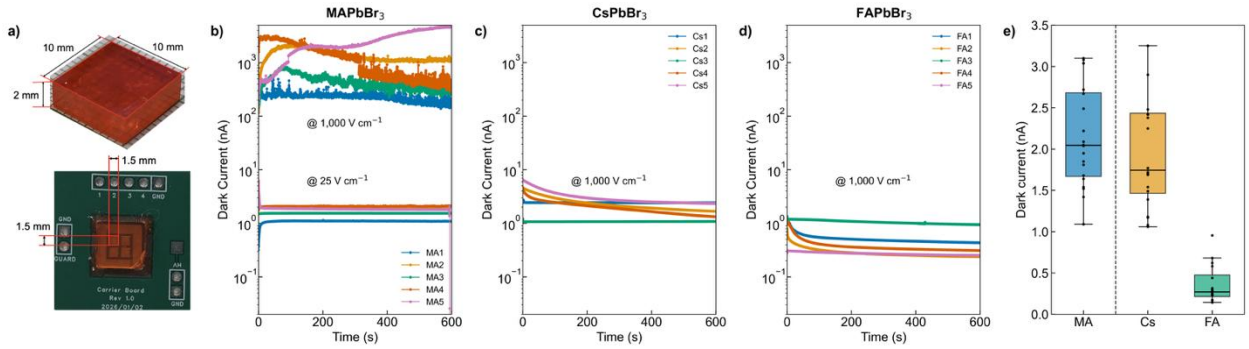


Figure 1. Dark-current characteristics. a) Photographs of a representative single crystal with dimensions indicated, and a crystal mounted on the evaluation board showing the pixel geometry and dimensions. b-d) Time evolution of dark current for b) $MAPbBr_3$ (relatively stable response at 25 V cm^{-1} but pronounced fluctuations at 1,000 V cm^{-1}), c) $CsPbBr_3$ (1,000 V cm^{-1}), and d) $FAPbBr_3$ (1,000 V cm^{-1}). Each trace represents one pixel from 5 independent crystals. e) Statistical distribution of stabilized dark current values for $MAPbBr_3$ (25 V cm^{-1}), $CsPbBr_3$ (1,000 V cm^{-1}) and $FAPbBr_3$ (1,000 V cm^{-1}), compiled from 20 devices per composition (5 crystals × 4 pixels per crystal). Box plots indicate the median (center line), interquartile range (box), and 1.5× interquartile range (whiskers); individual measurements are overlaid as points.

$MAPbBr_3$ devices exhibited a pronounced electric field-dependent I_{dark} instability. At 1,000 V cm^{-1}, the dark current continuously drifted with time (Fig. 1b), indicating strong ion migration and polarization effects. Correspondingly, the low-frequency charge-noise spectral density increased markedly with electric field (Supplementary Fig. 2a), resulting in *ENC* values approaching 5×10^6 e^- RMS at 1,000 V cm^{-1} (Supplementary Fig. 3a). Stable detector operation was therefore only possible at low electric field (25 V cm^{-1}), where the dark current partially stabilized and the electronic noise remained sufficiently low.

$CsPbBr_3$ devices exhibited improved operational stability. At 1,000 V cm^{-1}, the dark current remained relatively stable (Fig. 1c) together with *ENC* values of 4.5×10^3 e^- RMS (Supplementary

Fig. 2c). However, increasing electric field progressively enhanced the low-frequency noise contribution, producing *ENC* values approaching 5.6×10^4 e^- RMS at 4,000 V cm^{-1} (Supplementary Fig. 3c), indicating the onset of leakage-current fluctuations and polarization-related processes that increasingly limit detector performance at elevated bias.

$FAPbBr_3$ devices demonstrated the most favourable behaviour among all investigated compositions. At 1,000 V cm^{-1}, the dark current rapidly reached a stable plateau with minimal temporal drift (Fig. 1d). Moreover, the frequency-dependent noise spectra remained nearly unchanged with increasing bias (Supplementary Fig. 2b). The *ENC* remained near 2.6×10^3 e^- RMS at 1,000 V cm^{-1} and increased only slightly at 4,000 V cm^{-1} (Supplementary Fig. 3b), indicating strongly suppressed low-frequency noise and stable carrier transport under elevated electric field. Importantly, these *ENC* values are comparable to those required for practical low-dose direct-conversion X-ray imaging systems.[31,37]

The statistical distributions of stabilized I_{dark} and *ENC* are shown in Fig. 1e and Supplementary Fig. 3, with summarized values provided in Table 1. $FAPbBr_3$ devices exhibited both the lowest median dark current and a narrow device-to-device distribution (0.25 ± 0.11 nA), indicating excellent reproducibility and stability under high-field operation. In contrast, $CsPbBr_3$ and $MAPbBr_3$ devices showed comparatively broader I_{dark} distributions across independent devices. Furthermore, $MAPbBr_3$ exhibited acceptable *ENC* values only at low electric field (25 V cm^{-1}), whereas $FAPbBr_3$ maintained low and stable *ENC* values up to 4,000 V cm^{-1}. $CsPbBr_3$ displayed a monotonic increase in *ENC* and device-to-device variability with increasing bias. Collectively, these results reveal a strong composition dependence of electronic-noise stability and identify $FAPbBr_3$ as the most robust composition for high-field radiation-detector operation.

2.2. X-ray sensitivity

Based on the bias-dependent stability established above, X-ray sensitivity measurements were performed under steady-state bias for each device: $FAPbBr_3$ and $CsPbBr_3$ devices were evaluated at 1,000 V cm^{-1}, while $MAPbBr_3$ devices were measured at 25 V cm^{-1} to mitigate instability associated with ion migration. Sensitivity (*S*) was quantified from the slope of photocurrent density as a function of X-ray dose rate (Fig. 2b-d). A 70 kVp X-ray source was used for *S* measurements (Supplementary Fig. 4 and 5).

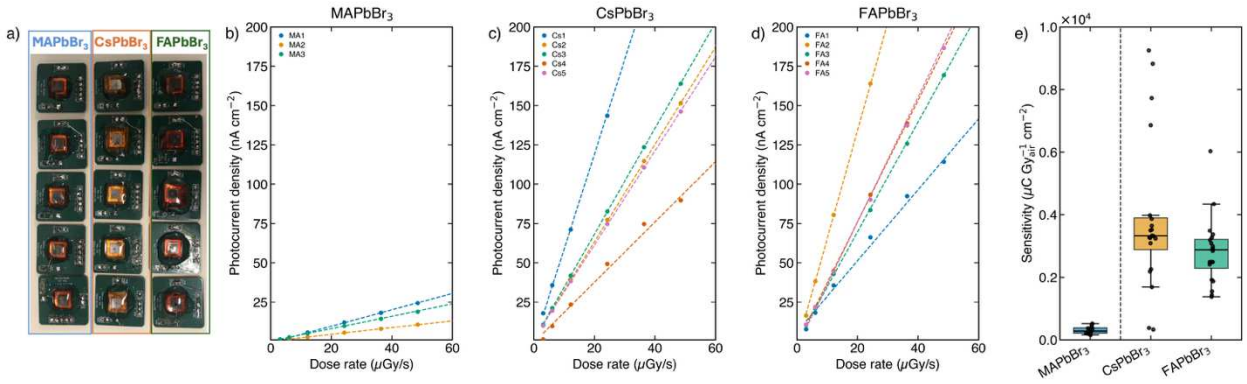


Figure 2. X-ray sensitivity. a) Photographs of all 15 individual single crystals mounted on PCB. b-d) Dose-rate-dependent photocurrent density for b) $MAPbBr_3$ (25 V cm^{-1}), c) $CsPbBr_3$ (1,000 V cm^{-1}), and d) $FAPbBr_3$ (1,000 V cm^{-1}). For clarity, only the highest-sensitivity pixel from each crystal (that is, the pixel exhibiting performance closest to the theoretical sensitivity limit) is shown. Spheres represent experimental measurements; dashed lines indicate linear fits used to extract sensitivity. e) Statistical distribution of steady-state sensitivity values for $MAPbBr_3$ (25 V cm^{-1}), $CsPbBr_3$ (1,000 V cm^{-1}) and $FAPbBr_3$ (1,000 V cm^{-1}). $MAPbBr_3$ statistics were compiled from 12 devices (3 crystals × 4 pixels per crystal), whereas $CsPbBr_3$ and $FAPbBr_3$ statistics were compiled from 20 devices each (5 crystals × 4 pixels per crystal). Box plots indicate the median (center line), interquartile range (box), and 1.5× interquartile range (whiskers); individual measurements are overlaid as points.

Of the 20 $MAPbBr_3$ devices, only 12 exhibited stable dose-rate-dependent photocurrent responses, yielding S of 280 ± 130 μC Gy_{air}^{-1} cm^{-2} (Fig. 2b). The limited number of stable devices and the substantially reduced S are consistent with the low-electric-field operation required for $MAPbBr_3$ (25 V cm^{-1}), which restricts carrier drift and limits charge collection efficiency.

$CsPbBr_3$ devices performed better, with S of 2,850 ± 620 μC Gy_{air}^{-1} cm^{-2} (Fig. 2c). Several devices operated near the theoretical limit (S_0) of ~5,000 μC Gy_{air}^{-1} cm^{-2} (estimated from absorbed X-ray energy and experimentally determined ionization energy, Supplementary Figure 5 and Methods). The remaining devices showed reduced performance, resulting in a broader device-to-device dispersion. This behaviour indicates increased variability in charge collection and transport among individual $CsPbBr_3$ devices.

$FAPbBr_3$ devices demonstrated higher *S*, reaching 3,300 ± 320 μC Gy_{air}^{-1} cm^{-2} (Fig. 2d), approaching their theoretical sensitivity limit. Moreover, $FAPbBr_3$ devices exhibited consistent performance with relatively narrow statistical dispersion, indicating excellent reproducibility under high-field operation.

To assess the contribution of photon absorption to the measured *S*, we calculated the spectrum-weighted X-ray absorption of a filtered 70 kVp spectrum for 2 mm-thick $MAPbBr_3$ and $FAPbBr_3$, and 1 to 2-mm-thick $CsPbBr_3$ crystals (Supplementary Fig. 4). The absorption was obtained by integrating the energy-dependent attenuation over the incident X-ray spectrum. For 2 mm crystals, the calculated absorption values were 94.4% for $MAPbBr_3$, 93.8% for $FAPbBr_3$, and 99.0% for $CsPbBr_3$, and even 1-mm-thick $CsPbBr_3$ retained 92.2% absorption. These results indicate that all investigated crystals provided near-complete photon absorption under the measurement conditions. Consequently, the observed variations in *S*, including those among $CsPbBr_3$ devices of different thicknesses, cannot be attributed primarily to differences in X-ray absorption, but instead originate from charge collection efficiency (*CCE*), as discussed below.

The statistical distributions of *S* across all compositions are shown in Fig. 2e and summarized in Table 1. $MAPbBr_3$ devices consistently exhibited low sensitivity, reflecting limited charge collection under low-electric-field operation. $CsPbBr_3$ devices showed intermediate sensitivity accompanied by comparatively large device-to-device variation, whereas $FAPbBr_3$ devices achieved the highest *S* and the closest approach to the theoretical limit. Deviations above and below the theoretical sensitivity arise from differences in carrier trapping, recombination, and contact-related transport losses. Defect- and surface-state-assisted localization of minority carriers can generate apparent photoconductive gain by creating an imbalance between excess minority and majority carrier populations and promoting accumulation of mobile majority carriers in the conduction channel.[38,39] Conversely, enhanced trap-assisted recombination, incomplete carrier extraction, and non-ideal contacts suppress charge collection efficiency and reduce the measured *S*.[7,40,41] Overall, these results indicate that detector performance is governed primarily by charge-transport and trapping dynamics rather than by photon absorption efficiency, consistent with the extrinsic origin of photoconductive gain and well-established dependence of photoconductor performance on charge-collection processes.[7,37–41]

2.3. Charge mobility-lifetime $(\mu\tau)_h$ product

To further elucidate the origin of the observed variations in X-ray sensitivity, the hole mobility-lifetime $(\mu\tau)_h$ product was extracted from representative pixels of each crystal using the electric-field-dependent *CCE* (Fig. 3). The $(\mu\tau)_h$ provides a direct measure of carrier drift length and *CCE*, enabling a quantitative link between the measured *S* and intrinsic transport properties.

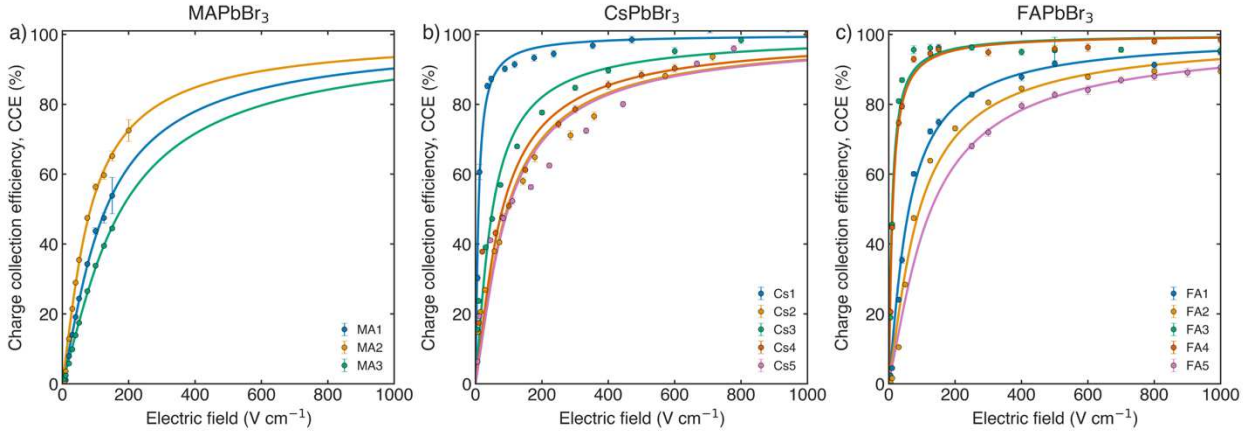


Figure 3. Electric-field-dependent *CCE* and Hecht model analysis. a-c) *CCE* as a function of electric field for a) $MAPbBr_3$, b) $CsPbBr_3$ and c) $FAPbBr_3$ devices. Points represent experimental measurements; solid curves are best fits to the Hecht equation.

For $MAPbBr_3$ devices, *CCE* measurements were limited to electric fields below ~150 V cm^{-1} (Fig. 3a), as operation at higher biases resulted in increased noise and current instabilities that exceeded the photocurrent signal. Notably, the *CCE* did not reach saturation within the accessible field range, indicating incomplete charge collection due to limited carrier transport. The corresponding median $(\mu\tau)_h$ value was only 0.96 $\times 10^{-3}$ cm^2 V^{-1}, consistent with the low *S* and transport-limited detector performance observed for $MAPbBr_3$.

$CsPbBr_3$ devices exhibited an improved transport characteristic, with a median $(\mu\tau)_h$ value of 1.2×10^{-3} cm^2 V^{-1} and a maximum value reaching 1.2×10^{-2} cm^2 V^{-1} (Fig. 3b). Several devices approached *CCE* saturation at moderate electric fields, consistent with the improved X-ray sensitivity compared with $MAPbBr_3$. However, the broad distribution of $\mu\tau$ values and the incomplete saturation observed for some devices indicate substantial device-to-device variability in carrier transport and trapping processes.

$FAPbBr_3$ devices exhibited the most favourable transport properties (Fig. 3c). The median reached 2.1×10^{-3} cm^2 V^{-1}, while the best-performing device exhibited a $(\mu\tau)_h$ value of 1.2×10^{-2} cm^2 V^{-1} for

the (Fig. 3b). These high $(\mu\tau)_h$ values resulted in rapid *CCE* saturation and sensitivities approaching the theoretical limit, demonstrating efficient charge transport and near-complete carrier collection under applied bias.

The statistical distributions of $(\mu\tau)_h$ values are summarized in Table 1, and are consistent with previously reported results for perovskite single crystals, which exhibit significantly enhanced charge transport compared to polycrystalline films due to reduced trap density and the absence of grain boundaries.[1,42,43] In particular, $(\mu\tau)_h$ values on the order of ~10^{-2} cm^2 V^{-1} have been reported for high-quality perovskite single crystals, approaching those of established semiconductor radiation detector materials.[42] The $(\mu\tau)_h$ analysis establishes carrier transport as the primary factor governing detector performance. Devices with high $(\mu\tau)_h$ values exhibit near-unity charge collection and sensitivity approaching the theoretical limit, motivating their subsequent evaluation using the industry-standard metric of zero-frequency detective quantum efficiency, *DQE*(0).

2.4. Detective quantum efficiency

The zero-frequency detective quantum efficiency (*DQE(0)*) was evaluated as a system-level figure of merit describing the preservation of the incident X-ray signal-to-noise ratio (*SNR*) by the detector.[31,44] In direct-conversion photoconductive detectors, the *DQE(0)* is governed by the combined effects of X-ray absorption, *CCE* and electronic noise.[19,45,46] Since all investigated compositions exhibit near-unity absorption under the 70 kVp spectrum used in this study (Supplementary Fig. 4), the practical detector performance is governed primarily by charge transport and electronic-noise characteristics rather than by photon absorption.

Experimentally measured $(\mu\tau)_h$ and *ENC* values were used to calculate *DQE(0)* for each detector using a cascaded direct-conversion detector model adapted from the Kabir-Kasap formalism (see Methods section for details).[37,47] The noise-equivalent dose (*NED*) was estimated for each device from the experimentally measured *ENC* values and calculated detection efficiency. To assess detector suitability for low-dose imaging, the detector dose required to achieve 95% of the maximum *DQE(0)*, denoted as $D_{0.95DQEmax}$, was estimated. Equivalent dose-per-image values assuming a representative integration time of 20 ms, corresponding to a 50 frames s^{-1} acquisition rate commonly used in high-speed fluoroscopic and dynamic X-ray imaging systems, are provided in Supplementary Fig. 6 and 7 for comparison with practical imaging conditions.[48–50]

Figure 4 presents the device-specific *DQE(0)* calculations as a function of incident detector dose rate using experimentally measured $(\mu\tau)_h$ products, detector thicknesses, spectrum-weighted X-ray absorption, and *ENC* values. Dashed lines denote the calculated *NED*, while dotted lines indicate the detector dose rate required to reach 95% of the maximum *DQE(0)*.

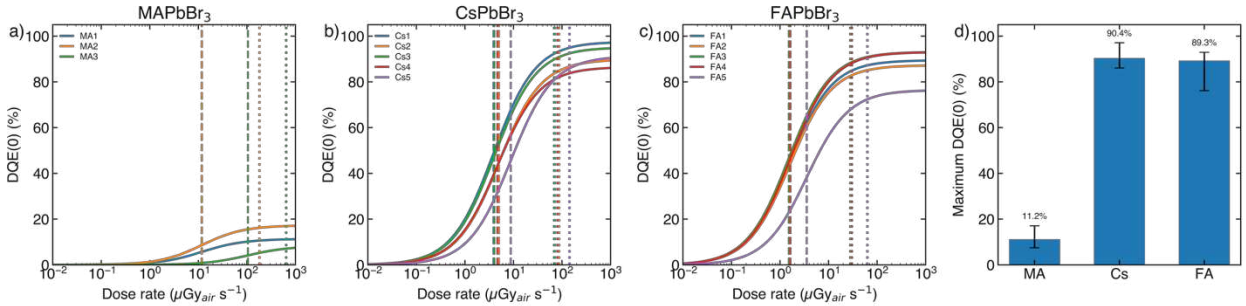


Figure. 4. Device-specific DQE(0). DQE(0) as a function of incident detector dose rate calculated from experimentally measured $(\mu\tau)_h$ products, detector thicknesses, spectrum-weighted X-ray absorption, and *ENC* values for a) $MAPbBr_3$, b) $CsPbBr_3$ and c) $FAPbBr_3$ devices. Dashed lines denote the calculated *NED*; dotted lines indicate the detector dose rate required to reach 95% of the maximum *DQE(0)*. d) Distribution of maximum *DQE(0)* values derived from device-by-device calculations.

$MAPbBr_3$ devices exhibited stable operation only at relatively low electric field (~25 V cm^{-1}). Although the *ENC* remained comparatively low, the limited $\mu\tau$ product resulted in incomplete charge collection and consequently low *DQE(0)* despite the high X-ray absorption (~94.4%). The median DQE_{max} reached only 11.3%, indicating strongly transport-limited detector performance. $MAPbBr_3$ devices also required the highest detector dose to approach quantum-limited operation, with $D_{0.95DQEmax}$ = 181.7 $\mu Gy_{air}\, s^{-1}$.

In contrast, $CsPbBr_3$ devices achieved substantially higher *DQE(0)* values owing to their improved charge-transport properties and near-complete X-ray absorption (~99%). The median DQE_{max} reached 90.4%; however, larger device-to-device variations in *ENC*, $(4.46\pm1.65)\times10^3$ e^- RMS, resulted in increased *NED* values of 4.66 $\mu Gy_{air}\, s^{-1}$ and a higher $D_{0.95DQEmax}$ of 81.4 $\mu Gy_{air}\, s^{-1}$. These results indicate that the performance of $CsPbBr_3$ devices is increasingly limited by electronic-noise fluctuations rather than by charge transport.

$FAPbBr_3$ devices combined enhanced carrier transport with low and highly reproducible electronic noise. As a result, the *DQE(0)* rapidly approached saturation, yielding a median DQE_{max} of 89.3%. $FAPbBr_3$ devices exhibited the lowest *NED* values, 1.6 $\mu Gy_{air}\ s^{-1}$, and required $D_{0.95DQEmax}$ of only 29.5 $\mu Gy_{air}\ s^{-1}$. Although the maximum *DQE(0)* values of $FAPbBr_3$ and $CsPbBr_3$ were nearly identical, the substantially lower *NED* and $D_{0.95DQEmax}$ of $FAPbBr_3$ demonstrate its superior potential for low-dose imaging performance.

We then compared these values with clinically relevant imaging conditions. According to the international standard IEC 62220-1, *DQE* evaluations are commonly performed at detector air kerma levels of 1-20 μGy under RQA5 beam quality conditions, a range comparable to that encountered in clinical digital radiography systems.[51] Both $FAPbBr_3$ and $CsPbBr_3$ reached near-saturated *DQE(0)* at detector exposures below or within this range, indicating that the detectors would operate near the quantum-noise limit under realistic radiographic and computed tomography imaging conditions.

The statistical distributions of DQE_{max}, *NED* and $D_{0.95DQEmax}$ are summarized in Table 1. Overall, the device-by-device *DQE(0)* analysis demonstrates that the practical detector performance in bromide perovskite single crystals is primarily governed by the interplay between charge transport and electronic-noise stability rather than by X-ray absorption. Among the investigated compositions, $FAPbBr_3$ provides the most favourable balance between efficient carrier extraction, low electronic noise, detector reproducibility, and low-dose imaging performance.

2.5. Photon-counting γ-ray spectroscopy

We next examined the performance of bromide perovskite crystals for photon-counting γ-ray spectroscopy under ^{57}Co source with 122.1 keV (85%) and 136.5 keV (11%) emission. Unlike X-ray measurements, γ-ray spectroscopy directly probes the response to individual photon interactions and therefore provides a stringent assessment of charge transport, electronic noise and energy discrimination. Moreover, the 122.1 and 136.5 keV γ-ray emissions of ^{57}Co closely bracket the 140 keV photopeak of ^{99m}Tc , the radionuclide most widely used in single-photon emission computed tomography (SPECT), making ^{57}Co an appropriate surrogate for evaluating the suitability of these materials for future semiconductor SPECT imaging.[49,52–55]

None of the $MAPbBr_3$ devices produced resolvable γ-ray spectra. At the electric fields required for photon-counting operation, the electronic noise exceeded the signal generated by individual γ-ray interactions, consistent with the limited charge-transport properties and poor high-field operation observed above. Consequently, $MAPbBr_3$ was not investigated further for γ-ray spectroscopy.

Figure 5 presents representative γ-ray spectra measured using $CsPbBr_3$ and $FAPbBr_3$ devices. $CsPbBr_3$ exhibited limited spectroscopic performance. Among the 20 investigated devices, only 2 produced clearly resolved ^{57}Co photopeaks, with energy resolutions of 14.8% and 17.6% at an electric field of 2,000 V cm^{-1}. During operation, the spectroscopic response progressively deteriorated under continuous bias, resulting in increased electronic noise and loss of photopeak definition after 24 h. Consequently, despite its favourable X-ray absorption and promising charge-transport properties, $CsPbBr_3$ did not demonstrate sufficiently reproducible performance for practical photon-counting γ-ray spectroscopy.

In contrast, all 20 $FAPbBr_3$ devices successfully resolved the 122.1 keV ^{57}Co photopeak following 24 h electrical pre-biasing at 4,000 V cm^{-1}, consistent with a recent report.[56] The detectors exhibited a median energy resolution of 6.1 ± 0.7%, with the best achieving 5.2%, demonstrating efficient charge transport, low electronic noise and excellent device-to-device reproducibility (Supplementary Fig. 8). Furthermore, 16 of the 20 devices clearly resolved the secondary 136.5 keV photopeak of ^{57}Co, demonstrating excellent energy discrimination over the energy range relevant to low-energy γ-ray spectroscopy and potential SPECT imaging applications. The ability to consistently resolve both photopeaks across independently fabricated detectors further highlights the excellent reproducibility of the $FAPbBr_3$ perovskite.

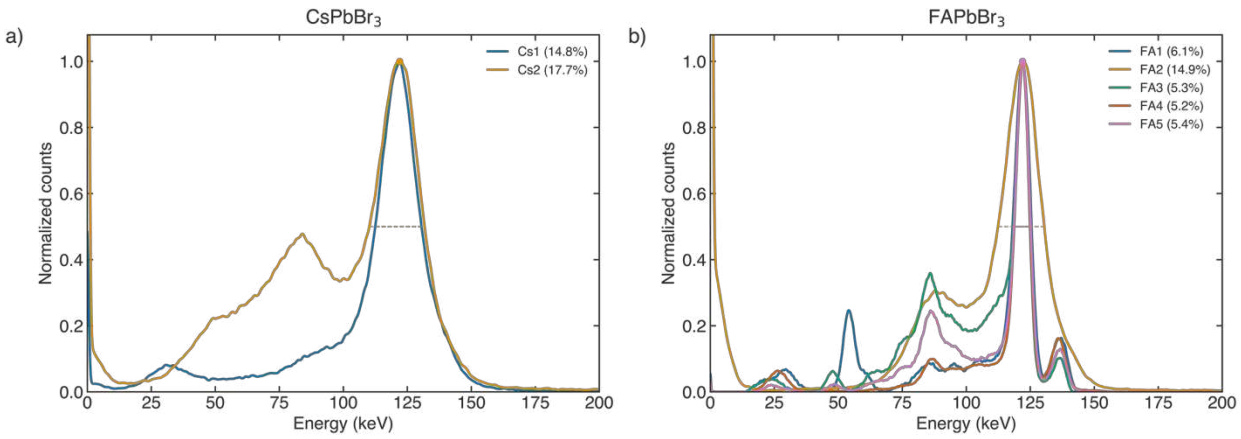


Fig 5. Photon-counting γ-ray spectroscopy using bromide perovskite single-crystal detectors. Normalized γ-ray spectra of a ^{57}Co source recorded with detectors based on a) $FAPbBr_3$ and b) $CsPbBr_3$.

To interpret the experimentally observed spectroscopic performance, we employed a detector-specific Monte Carlo charge-transport model parameterized using the experimentally measured detector thicknesses, mobility-lifetime products and equivalent noise charge values (see Methods). The calculated spectra accurately reproduced the measured photopeak positions (Supplementary Fig. 9), indicating that the model captures the dominant physical processes governing the detector response. Following this validation, the *ENC* was systematically reduced to values representative of modern low-noise ASIC and CMOS readout electronics while keeping the experimentally measured detector properties fixed: the simulations predict a substantial improvement in spectroscopic performance, with the best $FAPbBr_3$ detector approaching ~1% energy resolution at 122 keV (Supplementary Fig. 10). These results indicate that further improvements in readout electronics, rather than the detector material itself, may enable near-intrinsic energy resolution in bromide perovskite detectors.

Conclusions

In summary, we performed a statistically robust, device-by-device comparison of $MAPbBr_3$, $FAPbBr_3$, and $CsPbBr_3$ single-crystal detectors for X-ray and photon-counting γ-ray spectroscopy under identical fabrication and measurement conditions. By combining electrical characterization, mobility-lifetime analysis, X-ray sensitivity measurements, experimentally constrained *DQE(0)* calculation, photon-counting γ-ray spectroscopy and detector-parametrized Monte Carlo charge-

transport simulations, this work establishes a comprehensive framework for quantitatively comparing the detector performance of bromide perovskite single crystals.

Although, all investigated compositions exhibited near-unity X-ray absorption under the 70 kVp spectrum, detector performance was found to be governed predominantly by the interplay between charge transport and electronic-noise stability rather than photon attenuation. $MAPbBr_3$ exhibited pronounced field-dependent instability and incomplete charge collection, restricting operation to low electric field and preventing stable photon-counting detection. $CsPbBr_3$ achieved efficient X-ray absorption and high *DQE(0)* but increased electronic noise and device-to-device variability at high electric fields limited both low-dose imaging performance and reproducible γ-ray spectroscopy. In contrast, $FAPbBr_3$ consistently combined high $\mu\tau$, efficient charge collection, low electronic noise, and excellent device reproducibility. Consequently, $FAPbBr_3$ achieved the lowest *NED*, the lowest detector dose required to reach near-saturated *DQE(0)* and successfully resolved the ^{57}Co photopeak in all investigated devices, with a median energy resolution of $6.1 \pm 0.7\%$ and the best value of 5.2%.

This work identifies $FAPbBr_3$ as the most promising perovskite composition for direct-conversion radiation detection, providing an optimal balance between carrier transport electronic-noise performance, detector reproducibility, and operational stability. More broadly, this work establishes experimentally validated design principles for optimizing perovskite semiconductor detectors and provides a quantitative benchmark for the development of perovskite low-dose X-ray imagers, photon-counted computer tomography, γ-ray spectrometers, and SPECT imaging.

3. Methods

3.1. Device fabrication

$MAPbBr_3$, $FAPbBr_3$, and $CsPbBr_3$ single crystals were grown using a solution-based method reported previously.[32,33,57] Prior to device fabrication, the top and bottom facets of the crystals were mechanically polished to obtain flat, parallel surfaces and a target thickness of ~2 mm. Initial planarization was performed using a polishing machine, followed by sequential polishing with grit papers of decreasing particle size (2 μm, 1 μm, and 0.3 μm) on artificial felt. The crystals were subsequently cleaned in toluene to remove residual contaminants. Immediately prior to contact deposition, the crystal surfaces were subjected to chemical treatment for surface defect passivation, following established protocols.[56] After processing, the final thicknesses were ~2 mm for $MAPbBr_3$ and $FAPbBr_3$ crystals (devices M1-M5 and F1-F5), while $CsPbBr_3$ crystals (devices C1-C5) had thicknesses of 1.0, 1.4, 1.7, 1.8, and 2.0 mm, respectively. All detectors were fabricated using a consistent contact architecture (Supplementary Fig. 1). Gold (Au) contacts (80 nm) defining four pixels and a guard ring were deposited by thermal evaporation. A bismuth (Bi) anode (300 nm) was subsequently deposited by electron-beam evaporation.[58] The asymmetric Au/Bi electrode configuration was selected to induce a Schottky barrier, suppressing leakage current and reducing electronic noise.

Following electrode deposition, the crystals were mounted on custom-designed printed circuit boards (PCBs). Electrical connections between the top electrodes and PCB pads were established using copper wires and silver epoxy, and the assemblies were encapsulated with epoxy for mechanical stability. The detectors were housed in metallic enclosures equipped with connectors for electrical interfacing.

3.2. Electronic noise measurements under dark conditions

Electronic-noise measurements were performed under dark conditions using a CR-110-R2.2 charge-sensitive preamplifier (Cremat Inc.) connected to individual detector pixels. The detector output was measured using a Tektronix TDS3054C digital oscilloscope. Noise measurements were conducted at fixed electric fields corresponding to the detector operating conditions used for X-ray measurements.

The time-domain baseline fluctuations were exported as voltage traces and analyzed using Welch power spectral density estimation with a Hann window and 50% overlap[59]. The root-mean-square (RMS) baseline voltage fluctuation (σ_V) was determined from the time-domain signal:

$$\sigma_V = \sqrt{\frac{1}{N}\sum_{i=1}^{N}(V_i - \bar{V})^2} \quad (1)$$

where V_i is the instantaneous voltage value, $\bar{V}$ is the mean baseline voltage, and N is the total number of sampled points.

The *ENC* (Supplementary Fig. 2) was subsequently calculated according to:

$$ENC = \frac{\sigma_V}{G_Q \cdot q_e} \quad (2)$$

where *ENC* is expressed in electrons RMS (e^- RMS), G_Q is the charge-sensitive preamplifier gain (1.4 V pC^{-1} for the CR-110-R2.2 preamplifier), and q_e is the elementary charge (1.602×10^{-19} C).

The frequency-dependent charge-noise density (Supplementary Fig. 3) was obtained from the voltage-noise spectral density according to:

$$S_Q^{\frac{1}{2}}(f) = \frac{S_V^{\frac{1}{2}}(f)}{G_Q} \quad (3)$$

where $S_Q^{\frac{1}{2}}(f)$ is the equivalent charge-noise spectral density (e^- $Hz^{-1/2}$ or C $Hz^{-1/2}$), $S_V^{\frac{1}{2}}(f)$ is the voltage-noise spectral density measured from the oscilloscope (V $Hz^{-1/2}$), and f is frequency.

3.3. X-ray source

A Comet X-Ray System (Flamat, Switzerland) served as an X-ray source in this study. The mobility-lifetime $(\mu\tau)_h$ products were measured under X-ray irradiation at 40 kVp without additional filtration.[60]

X-ray sensitivity measurements were performed at 70 kVp, with the tube current adjusted to control the dose rate. 0.72 mm thick Cu and 6 mm thick Al were used as filters, and the source-to-detector distance was 100 cm. The corresponding filtered X-ray spectrum had a mean photon

energy of ~55 keV (Supplementary Fig. 4). Dose-rate calibration was performed using a calibrated PTW TN23342W ionization chamber (Supplementary Fig. 5).

3.4. Theoretical X-ray sensitivity

The following formula was used to calculate the theoretical sensitivity (S_0)[33]:

$$S_0 = \frac{\frac{\Phi}{X}\bar{E}\beta}{IE}q\eta \quad (4)$$

where $\bar{E}$ is the mean energy of X-ray photons (54.7 keV for 70 kVp source using a Cu and Al attenuators, as discussed above); Φ/X is the fluence per unit exposure (3.0644×10^{12} photons cm^{-2} Gy^{-1}); IE is the ionization energy (5.63 for $MAPbBr_3$, 5.35 for $FAPbBr_3$ and 5.36 for $CsPbBr_3$, Supplementary Fig. 11); β is the energy attenuation efficiency (100% theoretical limit); η is the charge collection efficiency (100% theoretical limit); and the S_0 were estimated to be approximately 4,770, 5,020, and 5,010 $\mu C\ Gy_{air}^{-1}\ cm^{-2}$ for $MAPbBr_3$, $FAPbBr_3$, and $CsPbBr_3$, respectively.

3.5. DQE evaluation

The zero-frequency detective quantum efficiency, *DQE(0)*, was calculated as a function of the incident detector dose rate (D), using experimentally measured charge-transport and electronic-noise parameters for each individual detector device. The charge collection efficiency (CCE) was estimated using the Hecht relation:

$$CCE(E) = \frac{\mu\tau E}{d}\left[1 - \exp\left(-\frac{d}{\mu\tau E}\right)\right] \quad (5)$$

where $\mu\tau$ is the mobility-lifetime product, E is the electric field, and d is the detector thickness.

The detection efficiency (DE) was calculated as the product of the spectrum-weighted X-ray absorption (A) and the charge collection efficiency:

$$DE = A \times CCE \quad (6)$$

Electronic-noise characterization was performed under dark conditions and under X-ray irradiation using a CR-10-R2.2 charge-sensitive preamplifier connected to individual detector pixels. The preamplifier output was recorded using a Tektronix TDS3054C digital oscilloscope. Frequency-

dependent charge-noise spectral densities were extracted using the Welch power spectral density analysis. Supplementary Fig. 12a shows the measured charge-noise spectral density under increasing X-ray dose rates for the $FAPbBr_3$ reference detector operated at 1,000 V cm^{-1}. Increasing dose rate produced progressively increasing low-frequency charge noise, while the high-frequency region remains dominated by electronic readout noise.

The root-mean-square (RMS) charge noise was extracted from the baseline fluctuations and plotted as a function of X-ray dose rate (Supplementary Fig. 12b). Linear fitting of the noise-dose dependence yielded the experimentally extracted reference noise-equivalent dose rate of NED_{ref} = 1.513 $\mu Gy_{air}\ s^{-1}$. The reference detector corresponded $FAPbBr_3$ (F3 device operated at 1,000 V cm^{-1}), which exhibited stable operation, low electronic noise, and the highest measured $\mu\tau$ product among the investigated devices, thereby providing a reliable reference for experimental noise characterization. The experimentally measured equivalent noise charge of this device was ENC_{ref} = 2,720 e^- RMS.

Device-specific noise-equivalent dose (*NED*) values were subsequently scaled according to experimentally measured *ENC* and calculated *DE*:

$$NED_i = NED_{ref}\left(\frac{ENC_i}{ENC_{ref}}\right)^2\left(\frac{DE_{ref}}{DE_i}\right) \tag{7}$$

where ENC_i and DE_i are the experimentally measured equivalent noise charge and calculated detection efficiency of device *i*, respectively.

The *DQE(0)* was calculated according to:

$$DQE(0) = \frac{DE}{1+\frac{NED}{D}} \tag{8}$$

where *D* is the incident detector dose rate expressed in $\mu Gy_{air}\ s^{-1}$. The dose rate required to achieve near-saturated detector performance was defined as the minimum dose satisfying:

$$DQE(0) \geq 0.95 \times DQE_{max} \tag{9}$$

This parameter was extracted individually for each detector device and reported as nGy_{air} $image^{-1}$, assuming a representative integration time of 20 ms. This conversion does not affect the DQE

calculation itself, which depends only on the total incident detector dose and not on the acquisition time. The reported values therefore provide a convenient image-based metric for comparison with practical radiographic imaging conditions.

3.6. Photon-counting γ-ray spectroscopy

Photon-counting γ-ray spectroscopy was performed to evaluate the single-photon detection capability of the bromide perovskite detectors. Individual detector pixels were connected to either a CR-100-R2.2 charge-sensitive preamplifier (Cremat Inc.) or an EV550 low-noise charge-sensitive preamplifier (Kromek Ltd.). The detectors were mounted on a modified CR-150-R6 evaluation board (Cremat Inc.) that enabled direct electrical connection to individual pixels (Supplementary Fig. 13 and 14). The preamplifier output was digitized using a CAEN DT5780M multichannel analyzer operated in pulse-height analysis mode. Energy spectra were acquired under irradiation from a sealed ^{57}Co source.

Energy calibration was performed using the 122.1 and 136.5 keV photopeaks of ^{57}Co, while the energy resolution (*ER* was determined from the full width at half maximum (FWHM) of the 122.1 keV photopeak according to

$$ER = \frac{FWHM}{E_{peak}} \times 100\% \quad (10)$$

3.7 Monte Carlo modeling of γ-ray spectroscopy

Monte Carlo modeling was performed to interpret the γ-ray spectroscopic performance of the detectors and to distinguish limitations arising from semiconductor charge transport from those imposed by the electronic readout noise. Unlike the experimental measurements, which include complete response of the detector and front-end electronics, the model enables independent evaluation of the contribution of charge collection and electronic noise to the measured energy resolution.

Incident ^{57}Co photons were sampled according to their emission probabilities, and photon interactions within the detector were simulated using stochastic interaction sampling based on energy-dependent linear attenuation coefficients calculated with the XrayPhysics library. Detector geometry, crystal composition, density and thickness corresponded to the experimentally

investigated $CsPbBr_3$ and $FAPbBr_3$ devices. The model included photoelectric absorption, Compton scattering, Pb characteristic fluorescence, and fluorescence escape.

For each interaction, the interaction depth was sampled from the exponential attenuation distribution, and the collected charge was calculated using the depth-dependent Hecht relation:

$$CCE(x) = \frac{\mu_e \tau_e E}{d}\left(1 - e^{-\frac{d-x}{\mu_e \tau_e E}}\right) + \frac{\mu_h \tau_h E}{d}\left(1 - e^{-\frac{x}{\mu_h \tau_h E}}\right) \quad (11)$$

where d is the detector thickness, E is the applied electric field, and $\mu\tau$ is the mobility-lifetime product.

The hole mobility-lifetime ($\mu_h\tau_h$) product was obtained experimentally from the Hecht analysis of the X-ray charge-collection measurements. Because independent measurements of the electron mobility-lifetime ($\mu_e\tau_e$) product were not available, the electron transport was varied between 0.6 and 1.0 times the experimentally measured hole value ($\mu_e\tau_e$ = (0.6 – 1.0) $\mu_h\tau_h$). This range reflects the comparable electron and hole transport commonly reported for bromide perovskite single crystals and was used to evaluate the sensitivity of the simulated spectra to the unknown electron transport parameter.[16,61,62] The simulations showed only minor changes in the predicted energy resolution across the range, indicating that the detector response is substantially more sensitive to electronic noise than to moderate variations in electron transport. Unless otherwise stated, $\mu_e\tau_e$ = $\mu_h\tau_h$ was used in the simulations.

The measured pulse height was calculated as

$$E_{meas} = CCE(x)E_{dep} \quad (12)$$

where E_{dep} is the deposited γ-ray energy.

Electronic noise was incorporated by Gaussian broadening using the experimentally measured equivalent noise charge:

$$\sigma_E = \frac{ENC \cdot IE}{1000} \quad (13)$$

where *ENC* is the equivalent noise charge, and *IE* is the electron-hole pair creation energy in the detector material.

Acknowledgements

S.V.D. acknowledges support from the National Research Council of Canada Industrial Research Assistance Program (NRC IRAP), which supported research and development activities at AY Sensors Inc. in sensor technologies and crystal processing. M.I.S. thanks the Natural Sciences and Engineering Research Council of Canada (RGPIN-2025-04895) and the Canada Research Chair Program (CRC-2024-00264) for financial support.

Conflict of Interest

M.I.S. is a co-founder of AY-Sensor Inc., which commercializes perovskite single crystals for radiation detection applications. The other authors declare no competing interests.

Author contributions

S.V.D. conceived and designed the project. V.Y., K.S., A.P.J., A.I.G. synthesized the crystals. S.V.D and V.Y. performed crystal preprocessing and device fabrication. S.T. provided guidance on the γ-ray spectroscopy methodology and contributed to the development of the γ-ray detection measurements. N.S. developed the electronic readout system for γ-ray spectroscopy measurements. D.K. measured the electronic noise of the devices. S.V.D and J.D. calculated the DQE of the devices. M.B.-C. and M.I.S. acquired resources. S.V.D. wrote the original draft of the manuscript. M.B.-C. and M.I.S. edited the manuscript. M.I.S. supervised the project.

References

(1) Wei, H.; Huang, J. Halide Lead Perovskites for Ionizing Radiation Detection. *Nat. Commun.* **2019**, *10* (1), 1066. https://doi.org/10.1038/s41467-019-08981-w.

(2) Saidaminov, M. I.; Abdelhady, A. L.; Murali, B.; Alarousu, E.; Burlakov, V. M.; Peng, W.; Dursun, I.; Wang, L.; He, Y.; Maculan, G.; Goriely, A.; Wu, T.; Mohammed, O. F.; Bakr, O. M. High-Quality Bulk Hybrid Perovskite Single Crystals within Minutes by Inverse Temperature Crystallization. *Nat. Commun.* **2015**, *6* (1), 7586. https://doi.org/10.1038/ncomms8586.

(3) Bao, C.; Chen, Z.; Fang, Y.; Wei, H.; Deng, Y.; Xiao, X.; Li, L.; Huang, J. Low-Noise and Large-Linear-Dynamic-Range Photodetectors Based on Hybrid-Perovskite Thin-Single-Crystals. *Adv. Mater.* **2017**, *29* (39), 1703209. https://doi.org/10.1002/adma.201703209.

(4) Musiienko, A.; Pipek, J.; Praus, P.; Brynza, M.; Belas, E.; Dryzhakov, B.; Du, M.-H.; Ahmadi, M.; Grill, R. Deciphering the Effect of Traps on Electronic Charge Transport Properties of Methylammonium Lead Tribromide Perovskite. *Sci. Adv.* **2020**, *6* (37), eabb6393. https://doi.org/10.1126/sciadv.abb6393.

(5) Kasap, S. O.; Zahangir Kabir, M.; Rowlands, J. A. Recent Advances in X-Ray Photoconductors for Direct Conversion X-Ray Image Detectors. *Curr. Appl. Phys.* **2006**, *6* (3), 288–292. https://doi.org/10.1016/j.cap.2005.11.001.

(6) Lutz, G. *Semiconductor Radiation Detectors*; Springer Berlin Heidelberg: Berlin, Heidelberg, 2007. https://doi.org/10.1007/978-3-540-71679-2.

(7) Owens, A.; Peacock, A. Compound Semiconductor Radiation Detectors. *Nucl. Instrum. Methods Phys. Res. Sect. Accel. Spectrometers Detect. Assoc. Equip.* **2004**, *531* (1), 18–37. https://doi.org/10.1016/j.nima.2004.05.071.

(8) Veale, M. C.; Bell, S. J.; Duarte, D. D.; Schneider, A.; Seller, P.; Wilson, M. D.; Iniewski, K. Measurements of Charge Sharing in Small Pixel CdTe Detectors. *Nucl. Instrum. Methods Phys. Res. Sect. Accel. Spectrometers Detect. Assoc. Equip.* **2014**, *767*, 218–226. https://doi.org/10.1016/j.nima.2014.08.036.

(9) Egan, C. K.; Jacques, S. D. M.; Wilson, M. D.; Veale, M. C.; Seller, P.; Beale, A. M.; Pattrick, R. a. D.; Withers, P. J.; Cernik, R. J. 3D Chemical Imaging in the Laboratory by Hyperspectral X-Ray Computed Tomography. *Sci. Rep.* **2015**, *5* (1), 15979. https://doi.org/10.1038/srep15979.

(10) Deumel, S.; van Breemen, A.; Gelinck, G.; Peeters, B.; Maas, J.; Verbeek, R.; Shanmugam, S.; Akkerman, H.; Meulenkamp, E.; Huerdler, J. E.; Acharya, M.; García-Batlle, M.; Almora, O.; Guerrero, A.; Garcia-Belmonte, G.; Heiss, W.; Schmidt, O.; Tedde, S. F. High-Sensitivity High-Resolution X-Ray Imaging with Soft-Sintered Metal Halide Perovskites. *Nat. Electron.* **2021**, *4* (9), 681–688. https://doi.org/10.1038/s41928-021-00644-3.

(11) Wu, H.; Ge, Y.; Niu, G.; Tang, J. Metal Halide Perovskites for X-Ray Detection and Imaging. *Matter* **2021**, *4* (1), 144–163. https://doi.org/10.1016/j.matt.2020.11.015.

(12) Yang, X.; Song, Y.; Wang, L.; Sun, Y.; Jin, B.; Wang, J.; Liu, H.; Yang, Y.; Lin, Q.; Fang, Y.; Dong, Q. In-Line Tempering Eliminates the Domain Boundary in Perovskite Single Crystals for High–Energy Resolution Ionizing Radiation Detectors. *Sci. Adv.* **2024**, *10* (51), eadq6866. https://doi.org/10.1126/sciadv.adq6866.

(13) Li, M.; Wang, S.; Wood, A.; Yeager, J. D.; Stepanoff, S. P.; Adler, J. C.; Shi, Z.; Wang, J.; Li, Z.; Wolfe, D. E.; Huang, J. Defect Repairing in Lead Bromide Perovskite Single

Crystals with Biasing and Bromine for X-Ray Photon-Counting Detectors. *Nat. Mater.* **2025**, *24* (12), 1993–2000. https://doi.org/10.1038/s41563-025-02310-x.
(14) Shrestha, S.; Tsai, H.; Nie, W. A Perspective on the Device Physics of Lead Halide Perovskite Semiconducting Detector for Gamma and X-Ray Sensing. *Appl. Phys. Lett.* **2023**, *122* (8), 080501. https://doi.org/10.1063/5.0138830.
(15) Tumen-Ulzii, G.; Salway, H.; Lu, Y.; Dubajic, M.; Doherty, T.; Bugby, S.; Dejene, F.; Lees, J.; Braddock, I.; Veale, M. C.; Wilson, M. D.; Anaya, M.; Stranks, S. D. Surface Passivated Perovskite Single Crystals for X-Ray Detectors with High Sensitivity. In *2024 IEEE Nuclear Science Symposium (NSS), Medical Imaging Conference (MIC) and Room Temperature Semiconductor Detector Conference (RTSD)*; IEEE: Tampa, FL, USA, 2024; pp 1–1. https://doi.org/10.1109/NSS/MIC/RTSD57108.2024.10656002.
(16) Dong, Q.; Fang, Y.; Shao, Y.; Mulligan, P.; Qiu, J.; Cao, L.; Huang, J. Electron-Hole Diffusion Lengths > 175 Mm in Solution-Grown CH3NH3PbI3 Single Crystals. *Science* **2015**, *347* (6225), 967–970. https://doi.org/10.1126/science.aaa5760.
(17) Shi, D.; Adinolfi, V.; Comin, R.; Yuan, M.; Alarousu, E.; Buin, A.; Chen, Y.; Hoogland, S.; Rothenberger, A.; Katsiev, K.; Losovyj, Y.; Zhang, X.; Dowben, P. A.; Mohammed, O. F.; Sargent, E. H.; Bakr, O. M. Low Trap-State Density and Long Carrier Diffusion in Organolead Trihalide Perovskite Single Crystals. *Science* **2015**, *347* (6221), 519–522. https://doi.org/10.1126/science.aaa2725.
(18) Kasap, S. Low-Cost X-Ray Detectors. *Nat. Photonics* **2015**, *9* (7), 420–421. https://doi.org/10.1038/nphoton.2015.108.
(19) Sakhatskyi, K.; Turedi, B.; Matt, G. J.; Wu, E.; Sakhatska, A.; Bartosh, V.; Lintangpradipto, M. N.; Naphade, R.; Shorubalko, I.; Mohammed, O. F.; Yakunin, S.; Bakr, O. M.; Kovalenko, M. V. Stable Perovskite Single-Crystal X-Ray Imaging Detectors with Single-Photon Sensitivity. *Nat. Photonics* **2023**, *17* (6), 510–517. https://doi.org/10.1038/s41566-023-01207-y.
(20) Sakhatskyi, K.; Bhardwaj, A.; Matt, G. J.; Yakunin, S.; Kovalenko, M. V. A Decade of Lead Halide Perovskites for Direct-Conversion X-Ray and Gamma Detection: Technology Readiness Level and Challenges. *Adv. Mater.* **2025**, *37* (27), 2418465. https://doi.org/10.1002/adma.202418465.
(21) Liu, D.; Guan, H.; Yan, Z.; Ma, L.; Hu, Q.; Liu, G.; Xiao, J. High-Performance CsPbBr3 Perovskite Single Crystals for Gamma-Ray Detection. *Adv. Photonics Nexus* **2026**, *5* (3), 034002. https://doi.org/10.1117/1.APN.5.3.034002.
(22) Neal, T. H.; Sandor, N.; Day, J.; Bazalova-Carter, M.; Saidaminov, M. I. Perovskite Photon-Counting Detectors: Narrowing the Field. *Chem. Mater.* **2026**, *38* (4), 1566–1576. https://doi.org/10.1021/acs.chemmater.5c02948.
(23) Haruta, Y.; Huber, P.; Hart, A.; Bazalova-Carter, M.; Saidaminov, M. I. The Effect of Air Ionization in Testing Perovskite-Based Direct Conversion X-Ray Detectors. *ACS Energy Lett.* **2024**, *9* (1), 271–274. https://doi.org/10.1021/acsenergylett.3c02399.
(24) Benadia, A. G.; Pan, L.; Bayikadi, K. S.; Liu, Z.; Peters, J. A.; Snyder, G. J.; Kanatzidis, M. G. Progress in Solution Growth of Cuboid $CsPbBr_3$ Single Crystals with Low Defect Densities and High-Sensitivity X-Ray Detection. *Cryst. Growth Des.* **2025**, *25* (21), 9288–9299. https://doi.org/10.1021/acs.cgd.5c01107.
(25) Pan, L.; Shrestha, S.; Taylor, N.; Nie, W.; Cao, L. R. Determination of X-Ray Detection Limit and Applications in Perovskite X-Ray Detectors. *Nat. Commun.* **2021**, *12* (1), 5258. https://doi.org/10.1038/s41467-021-25648-7.

(26) Gunawan, O.; Pae, S. R.; Bishop, D. M.; Virgus, Y.; Noh, J. H.; Jeon, N. J.; Lee, Y. S.; Shao, X.; Todorov, T.; Mitzi, D. B.; Shin, B. Carrier-Resolved Photo-Hall Effect. *Nature* **2019**, *575* (7781), 151–155. https://doi.org/10.1038/s41586-019-1632-2.
(27) Zhou, Y.; Fei, C.; Uddin, M. A.; Zhao, L.; Ni, Z.; Huang, J. Self-Powered Perovskite Photon-Counting Detectors. *Nature* **2023**, *616* (7958), 712–718. https://doi.org/10.1038/s41586-023-05847-6.
(28) Tsai, H.; Liu, F.; Shrestha, S.; Fernando, K.; Tretiak, S.; Scott, B.; Vo, D. T.; Strzalka, J.; Nie, W. A Sensitive and Robust Thin-Film x-Ray Detector Using 2D Layered Perovskite Diodes. *Sci. Adv.* **2020**, *6* (15), eaay0815. https://doi.org/10.1126/sciadv.aay0815.
(29) Shabbir, B.; Yu, J. C.; Warnakula, T.; Ayyubi, R. A. W.; Pollock, J. A.; Hossain, M. M.; Kim, J.; Macadam, N.; Ng, Leonard. W. T.; Hasan, T.; Vak, D.; Kitchen, M. J.; Jasieniak, J. J. Printable Perovskite Diodes for Broad-Spectrum Multienergy X-Ray Detection. *Adv. Mater.* **2023**, *35* (20), 2210068. https://doi.org/10.1002/adma.202210068.
(30) Jiang, J.; Xiong, M.; Fan, K.; Bao, C.; Xin, D.; Pan, Z.; Fei, L.; Huang, H.; Zhou, L.; Yao, K.; Zheng, X.; Shen, L.; Gao, F. Synergistic Strain Engineering of Perovskite Single Crystals for Highly Stable and Sensitive X-Ray Detectors with Low-Bias Imaging and Monitoring. *Nat. Photonics* **2022**, *16* (8), 575–581. https://doi.org/10.1038/s41566-022-01024-9.
(31) Sakhatskyi, K.; Bartosh, V.; Zhou, Y.; Matt, G. J.; Zhao, J.; Yakunin, S.; Huang, J.; Kovalenko, M. V. Characterizing Emerging Detector Materials for Low-Dose X-Ray Imaging. *Adv. Mater.* **2025**, *37* (45), e12795. https://doi.org/10.1002/adma.202512795.
(32) Haruta, Y.; Ye, H.; Huber, P.; Sandor, N.; Pavesic Junior, A.; Dayneko, S.; Qiu, S.; Yeddu, V.; Saidaminov, M. I. Reproducible High-Quality Perovskite Single Crystals by Flux-Regulated Crystallization with a Feedback Loop. *Nat. Synth.* **2024**, *3* (10), 1212–1220. https://doi.org/10.1038/s44160-024-00576-8.
(33) Pretto, T.; Dayneko, S.; Pavesic Junior, A.; Sandor, N.; Hart, A.; Haruta, Y.; Bazalova-Carter, M.; Santos, M. J. L.; Saidaminov, M. I. Flux-Regulated Crystallization of Perovskites Using Machine Learning-Predicted Solvent Evaporation Rates for X-Ray Detectors. *Adv. Funct. Mater.* **2026**, *36* (21), 2506188. https://doi.org/10.1002/adfm.202506188.
(34) Pecunia, V.; Anthopoulos, T. D.; Armin, A.; Bouthinon, B.; Caironi, M.; Castellanos-Gomez, A.; Chen, Y.; Cho, K.; Clegg, C.; Fang, X.; Fendel, P.; Fowler, B.; Gelinck, G.; Gottlob, H.; Guyot-Sionnest, P.; Hannebauer, R.; Hernandez-Sosa, G.; Hersam, M. C.; Hirsch, L.; Ho, J. C.; Isikgor, F. H.; Joimel, J.; Kim, H. J.; Konstantatos, G.; Labram, J.; Lemme, M. C.; Leo, K.; Lhuillier, E.; Lidorikis, E.; Loi, M. A.; Malinowski, P. E.; Merken, P.; Mueller, T.; Nasrollahi, B.; Natali, D.; Ng, T. N.; Nguyen, T.-Q.; Park, S. K.; Peng, L.-M.; Samorì, P.; Sargent, E. H.; Shen, L.; Shishido, S.; Shorubalko, I.; Sonar, P.; Stranks, S. D.; Tedde, S. F.; Vandewal, K.; Verhaegen, M.; Walia, S.; Yan, F.; Yokota, T.; Zhang, F. Guidelines for Accurate Evaluation of Photodetectors Based on Emerging Semiconductor Technologies. *Nat. Photonics* **2025**, *19* (11), 1178–1188. https://doi.org/10.1038/s41566-025-01759-1.
(35) Calado, P.; Telford, A. M.; Bryant, D.; Li, X.; Nelson, J.; O'Regan, B. C.; Barnes, P. R. F. Evidence for Ion Migration in Hybrid Perovskite Solar Cells with Minimal Hysteresis. *Nat. Commun.* **2016**, *7* (1), 13831. https://doi.org/10.1038/ncomms13831.
(36) Rey, S.; Lédée, F.; Freychet, G.; Vaxelaire, N.; Ihrenberger, J.; Gros Daillon, E.; Lombard, S.; Anglade, C.; Emieux, F.; Gergaud, P.; Grenet, L. Quantification of the Ionic Migration

Rates in Thick CsPbBr3 Films Revealed by Operando X-Ray Fluorescence. *Appl. Phys. Lett.* **2025**, *126* (11), 113502. https://doi.org/10.1063/5.0249790.
(37) Kabir, M. Z.; Kasap, S. O.; Zhao, W.; Rowlands, J. A. Direct Conversion X-Ray Sensors: Sensitivity, DQE and MTF. *IEE Proc. - Circuits Devices Syst.* **2003**, *150* (4), 258–266. https://doi.org/10.1049/ip-cds:20030663.
(38) Dan, Y.; Zhao, X.; Chen, K.; Mesli, A. A Photoconductor Intrinsically Has No Gain. *ACS Photonics* **2018**, *5* (10), 4111–4116. https://doi.org/10.1021/acsphotonics.8b00805.
(39) Vrucinic, N.; Zhang, Y. Reexamination of Gain Theory for Intrinsic Photoconductive Devices. *Photonics* **2025**, *12* (5), 523. https://doi.org/10.3390/photonics12050523.
(40) Stranks, S. D.; Burlakov, V. M.; Leijtens, T.; Ball, J. M.; Goriely, A.; Snaith, H. J. Recombination Kinetics in Organic-Inorganic Perovskites: Excitons, Free Charge, and Subgap States. *Phys. Rev. Appl.* **2014**, *2* (3), 034007. https://doi.org/10.1103/PhysRevApplied.2.034007.
(41) Kasap, S.; Frey, J. B.; Belev, G.; Tousignant, O.; Mani, H.; Greenspan, J.; Laperriere, L.; Bubon, O.; Reznik, A.; DeCrescenzo, G.; Karim, K. S.; Rowlands, J. A. Amorphous and Polycrystalline Photoconductors for Direct Conversion Flat Panel X-Ray Image Sensors. *Sensors* **2011**, *11* (5), 5112–5157. https://doi.org/10.3390/s110505112.
(42) Wei, H.; Fang, Y.; Mulligan, P.; Chuirazzi, W.; Fang, H.-H.; Wang, C.; Ecker, B. R.; Gao, Y.; Loi, M. A.; Cao, L.; Huang, J. Sensitive X-Ray Detectors Made of Methylammonium Lead Tribromide Perovskite Single Crystals. *Nat. Photonics* **2016**, *10* (5), 333–339. https://doi.org/10.1038/nphoton.2016.41.
(43) Yakunin, S.; Sytnyk, M.; Kriegner, D.; Shrestha, S.; Richter, M.; Matt, G. J.; Azimi, H.; Brabec, C. J.; Stangl, J.; Kovalenko, M. V.; Heiss, W. Detection of X-Ray Photons by Solution-Processed Lead Halide Perovskites. *Nat. Photonics* **2015**, *9* (7), 444–449. https://doi.org/10.1038/nphoton.2015.82.
(44) Dunham, B.; Motakef, S.; Datta, A. Performance of Hybrid and All-Inorganic Perovskite Direct X-Ray Imagers: Surpassing Commercial Standards. *Adv. Mater. Technol.* **2026**, *11* (6), e01491. https://doi.org/10.1002/admt.202501491.
(45) Bartosh, V.; Sakhatskyi, K.; Matt, G. J.; Kanak, A.; Bhardwaj, A.; Ferraresi, L. J. A.; Yakunin, S.; Kovalenko, M. V. High-Spatial-Resolution, Melt-Cast Perovskite X-Ray Imager. *Matter* **2026**, *9* (2). https://doi.org/10.1016/j.matt.2025.102600.
(46) Tanguay, J.; Richtsmeier, D.; Dydula, C.; Day, J. A.; Iniewski, K.; Bazalova-Carter, M. A Detective Quantum Efficiency for Spectroscopic X-Ray Imaging Detectors. *Med. Phys.* **2021**, *48* (11), 6781–6799. https://doi.org/10.1002/mp.15194.
(47) Kasap, S. O.; Rowlands, J. A. Direct-Conversion Flat-Panel X-Ray Image Sensors for Digital Radiography. *Proc. IEEE* **2002**, *90* (4), 591–604. https://doi.org/10.1109/JPROC.2002.1002529.
(48) Bushberg, J. T.; Seibert, J. A.; Leidholdt, E. M. J.; Boone, J. M. *The Essential Physics of Medical Imaging*, 3rd edition.; Wolters Kluwer Health/Lippincott Williams & Wilkins: Philadelphia, 2012.
(49) *Handbook of Medical Imaging, Volume 1. Physics and Psychophysics*; Van Metter, R. L., Beutel, J., Kundel, H. L., Eds.; SPIE, 2000. https://doi.org/10.1117/3.832716.
(50) Kalender, W. A. *Computed Tomography: Fundamentals, System Technology, Image Quality, Applications*, 3., revised edition.; Publicis Publishing: Erlangen, 2011.
(51) Illers, H.; Buhr, E.; Bergmann, D.; Hoeschen, C. Measurement of the Detective Quantum Efficiency (DQE) of Digital x-Ray Imaging Devices According to the Standard IEC 62220-

1; Yaffe, M. J., Flynn, M. J., Eds.; San Diego, CA, 2004; p 177. https://doi.org/10.1117/12.535999.
(52) Takahashi, T.; Watanabe, S. Recent Progress in CdTe and CdZnTe Detectors. *IEEE Trans. Nucl. Sci.* **2001**, *48* (4), 950–959. https://doi.org/10.1109/23.958705.
(53) Lee, W. W.; K-SPECT Group. Clinical Applications of Technetium-99m Quantitative Single-Photon Emission Computed Tomography/Computed Tomography. *Nucl. Med. Mol. Imaging* **2019**, *53* (3), 172–181. https://doi.org/10.1007/s13139-019-00588-9.
(54) Bakos, A.; Libor, L.; Urbán, S.; Géczi, T.; Bukva, M.; Hőhn, J.; Lázár, G.; Nagy, A.; Farkas, I.; Sipka, G.; Pávics, L.; Besenyi, Z. Dynamic [99mTc]Tc-Mebrofenin SPECT/CT in Preoperative Planning of Liver Resection: A Prospective Study. *Sci. Rep.* **2024**, *14* (1), 30305. https://doi.org/10.1038/s41598-024-81331-z.
(55) Cherry, S. R.; Sorenson, J. A.; Phelps, M. E. *Physics in Nuclear Medicine*, 4th ed.; Elsevier/Saunders: Philadelphia, 2012.
(56) Zhao, L.; Shi, Z.; Zhou, Y.; Wang, X.; Xian, Y.; Dong, Y.; Reid, O.; Ni, Z.; Beard, M. C.; Yan, Y.; Huang, J. Surface-Defect-Passivation-Enabled near-Unity Charge Collection Efficiency in Bromide-Based Perovskite Gamma-Ray Spectrum Devices. *Nat. Photonics* **2024**, *18* (3), 250–257. https://doi.org/10.1038/s41566-023-01356-0.
(57) Zhumekenov, A. A.; Saidaminov, M. I.; Haque, M. A.; Alarousu, E.; Sarmah, S. P.; Murali, B.; Dursun, I.; Miao, X.-H.; Abdelhady, A. L.; Wu, T.; Mohammed, O. F.; Bakr, O. M. Formamidinium Lead Halide Perovskite Crystals with Unprecedented Long Carrier Dynamics and Diffusion Length. *ACS Energy Lett.* **2016**, *1* (1), 32–37. https://doi.org/10.1021/acsenergylett.6b00002.
(58) He, Y.; Petryk, M.; Liu, Z.; Chica, D. G.; Hadar, I.; Leak, C.; Ke, W.; Spanopoulos, I.; Lin, W.; Chung, D. Y.; Wessels, B. W.; He, Z.; Kanatzidis, M. G. CsPbBr3 Perovskite Detectors with 1.4% Energy Resolution for High-Energy γ-Rays. *Nat. Photonics* **2021**, *15* (1), 36–42. https://doi.org/10.1038/s41566-020-00727-1.
(59) *welch — SciPy v1.17.0 Manual*. https://docs.scipy.org/doc/scipy/reference/generated/scipy.signal.welch.html?utm_source=chatgpt.com (accessed 2026-05-12).
(60) Bazalova-Carter, M.; Esplen, N. On the Capabilities of Conventional X-Ray Tubes to Deliver Ultra-High (FLASH) Dose Rates. *Med. Phys.* **2019**, *46* (12), 5690–5695. https://doi.org/10.1002/mp.13858.
(61) Stranks, S. D.; Eperon, G. E.; Grancini, G.; Menelaou, C.; Alcocer, M. J. P.; Leijtens, T.; Herz, L. M.; Petrozza, A.; Snaith, H. J. Electron-Hole Diffusion Lengths Exceeding 1 Micrometer in an Organometal Trihalide Perovskite Absorber. *Science* **2013**, *342* (6156), 341–344. https://doi.org/10.1126/science.1243982.
(62) Herz, L. M. Charge-Carrier Dynamics in Organic-Inorganic Metal Halide Perovskites. *Annu. Rev. Phys. Chem.* **2016**, *67* (Volume 67, 2016), 65–89. https://doi.org/10.1146/annurev-physchem-040215-112222.

Supplementary Files

This is a list of supplementary files associated with this preprint. Click to download.

- SupplementarySpreadsheet.xlsx
- SI260718.pdf